Capturing Coupled Structural and Electronic Motions During Excited-State Intramolecular Proton Transfer via Computational Multi-edge Resonant Inelastic X-ray Scattering

Amke Nimmrich,[†] Niranjan Govind,[*,‡] and Munira Khalil[*,†]

† *Department of Chemistry, University of Washington, WA-98195 Seattle, USA*

‡*Physical and Computational Sciences Directorate, Pacific Northwest National Laboratory,*
Richland, Washington 99352, USA

E-mail: niri.govind@pnnl.gov; mkhalil@uw.edu

Abstract

1

2   Proton transfer processes build the foundation of many chemical processes. In

3 excited state intramolecular proton transfer (ESIPT) processes, the ultrafast proton

4 transfer is impulsively initiated through light. Here, we explore the time-dependent

5 coupled atomic and electronic motions during and following ESIPT through computa-

6 tional time-resolved resonant inelastic X-ray scattering (RIXS). Excited-state ab initio

7 molecular dynamics simulations combined with time-dependent density functional the-

8 ory calculations were performed for a model ESIPT complex, 10-hydroxybenzo[h]quinoline,

9 to obtain transient RIXS signatures. The RIXS spectra at both the nitrogen and oxy-

10 gen K-edges were computed to resolve the electronic and atomic structural dynamics

11 from both the proton donor and acceptor perspective. The results demonstrate that

1

RIXS provides unprecedented details of the local electronic structure, the coupling between different core and valence excited electronic states, and the reorganization of the electronic structure coupled to the proton transfer process. We also develop a spectroscopic ruler correlating spectral shifts of a RIXS peak to the proton transfer distance during ESIPT. This work highlights the exciting potential of time resolved RIXS experiments at newly commissioned soft X-ray free electron laser facilities in measuring coupled electronic and structural changes during ultrafast chemical processes.

Proton transfer reactions are at the heart of many chemical and biological processes. Excited state intramolecular proton transfer (ESIPT) is a subclass of proton transfer processes where the proton transfer takes place on an electronically excited state after photoexcitation. The earliest reports of ESIPT date back to the 1950s when Weller observed a Stokes shift in the emission spectrum of salicylic acid, which he assigned to proton transfer from the hydroxy to the carboxy group following photo-excitation.[1] The fluorescence properties of ESIPT systems have led to their application in bioimaging (fluorescence markers) and optoelectronics, including preparation of white-light emitting dyads or production of organic light-emitting diodes.[2–4] The variety of applications for molecules undergoing ESIPT is dependent on the wide tunability of their optoelectronic properties requiring a molecular level understanding of the underlying ESIPT photophysics.

The intramolecular H-bonded complex, 10-hydroxybenzo[h]quinoline (HBQ), has served as an excellent model system to study the photophysics of ultrafast ESIPT processes and it has been the subject of intense experimental and theoretical efforts over the last two decades.[5–17] Fig. 1 shows an overview of the ESIPT process for the enol-keto transition in HBQ which is found preferentially in its enol form on the ground electronic state when in solution.[18] Previous spectroscopic studies have shown that upon excitation with 400 nm, ESIPT from E* to K* takes place within 13 fs.[19,20] The fluorescence from K* is red-shifted from the absorption by about 250 nm.[19] Interestingly, the absorption and emission wavelengths, efficiency and timescales of proton transfer and the ground state enol-keto equilibrium of

2

HBQ can be significantly altered by changing the substituents on the molecular backbone and varying the solvent environment.[18,21] A detailed understanding of the local electronic structure on the ground and excited states of HBQ is required as a function of its molecular structure to assess the impact of synthetic tuning on the photophysics of HBQ.
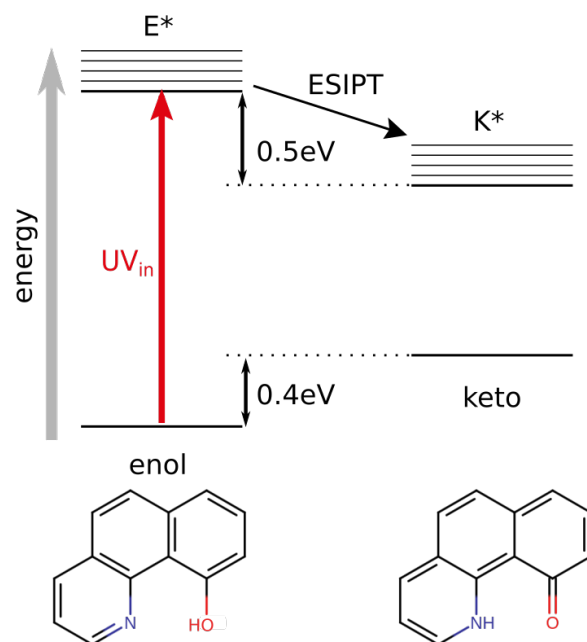
Figure 1. Schematic representation of the electronic states involved in the ESIPT process of HBQ during the enol (E) to keto (K) transformation. Excitation with UV light (UV_{in}) leads to population of the E* state from where ultrafast ESIPT to the K* state takes place within 13 fs. The energy difference between E and K and E* and K* were obtained from ground-state DFT and excited-state TDDFT calculations, respectively.

X-ray spectroscopies are element-specific, giving direct information on the local electronic structure near an atom of interest by tuning to its respective absorption edge. In the soft X-ray regime, this allows researchers to directly probe the local electronic and structural environment around carbon, oxygen or nitrogen atoms in organic molecules. With the availability of third-generation synchrotrons and advanced sample delivery systems, soft X-ray absorption near edge spectroscopy (XANES) has been used to investigate liquid and solution phase samples.[22–25] Both experimental and theoretical studies highlight the potential of soft X-ray XANES to study H-bonding in a variety of systems, including water, alcohols and

3

aqueous solutions of organic molecules.[26–29] Additionally, the intricate insights into the electronic structure from XANES enable a deeper understanding of solvent effects at a molecular level[30,31] and of the molecular orbitals and molecular stability of organic molecules.[32]

While XANES provides important insights on unoccupied electronic states, it does not contain information on occupied electronic states and the coupling between core and valence excited states. To obtain additional information on these properties, resonant inelastic X-ray scattering (RIXS) has received increasing attention for liquid and solution phase samples.[22,33,34] RIXS is a 2D X-ray spectroscopic technique that has the potential to reveal rich details of the electronic structure of molecules and materials by measuring the coupling between different electronic states.[35] The RIXS process is schematically explained in Fig. 2a. The incoming X-ray photon (X-ray$_{in}$) leads to excitation into a core excited state (CES, grey arrow) from where relaxation into a valence excited state (VES) via inelastic scattering, or back into the ground state (GS) via elastic scattering leads to the emission of an outgoing photon, X-ray$_{out}$ (dark red arrows). The CESs are defined as states in which an electron has been excited from either the nitrogen or oxygen 1s core orbital into the lowest unoccupied molecular orbitals, depending on the energy of X-ray$_{in}$. The VESs are states in which an electron has been excited from one of the highest occupied molecular orbitals into one of the lowest unoccupied molecular orbitals. For inelastic scattering, the difference between incoming and outgoing photon energy ($E_{trans} \neq 0$) contains information on the relative energies of the VESs involved in the transitions and their coupling to different CESs. Theoretically, RIXS can be described using the Kramers-Heisenberg equation[36] as described elsewhere.[37–40] The coupled electronic and structural insights from soft X-ray RIXS have previously been used to experimentally and computationally investigate the H-bonding structure of water in different phases,[41–46] distinguish different bonding characters,[32,47–49] as well as to observe solvent effects on the electronic structure of solutes[31] and more recently, to gain direct structural insight into structural dynamics on a molecular level in H-bonded systems[50] and single-molecule magnets.[51]

4

With the advent of X-ray free electron lasers (XFELs) operating in the soft x-ray regime, time-resolved RIXS and XANES experiments have become experimentally feasible and will continue to expand to a wider range of systems with further improvements at XFEL facilities, including the shift to higher repetition rates. Previous femtosecond RIXS experiments monitored the time-dependent changes in electronic structure in real time at the Fe L-edge[33,52,53] and the N K-edge[54] in transition metal complexes. Transient RIXS has also been used to probe excited state time-dependent hydrogen bonding interactions during a photoinduced thione-thiol tautomerization reaction.[49] By directly probing proton donor or acceptor sites, transient soft X-ray spectroscopies can be used to investigate the hydrogen bonding during proton transfer reactions. The continued development of computational methods to accurately model soft X-ray spectroscopy is crucial to the success of time-resolved X-ray spectroscopy.[55–58]

In a previous computational study from our group by Loe and co-workers, we investigated the time-resolved XANES signatures of HBQ during the ESIPT process.[8] The results showed transient features of HBQ at the O and N K-edges including the appearance of an additional peak and observation of time-dependent oscillations in the spectral features. The study provided valuable insights into the coupled electronic and atomic motions during ultrafast ESIPT in HBQ from the perspective of the H-bond donor and acceptor atoms. Here, we compute transient RIXS spectra of HBQ, presenting the first RIXS study simulating the time-resolved spectral signatures at the N and O K-edges during and following the ultrafast ESIPT process. Our work reveals how the transient RIXS features encode time-evolving electronic state couplings as a function of the proton transfer and we develop a spectroscopic ruler to connect spectral energy shifts to proton transfer distance.

Figure 2b shows XANES spectra of HBQ in its enol form at the N (top panel) and O (bottom panel) K-edges. We note that the spectra presented here, are shifted by $11\,\mathrm{eV}$ to match theory and experimental data for similar compounds (see Fig. S1 and S2 in the SI). The XANES spectra at the N and O K-edges of organic complexes, like HBQ, are

5
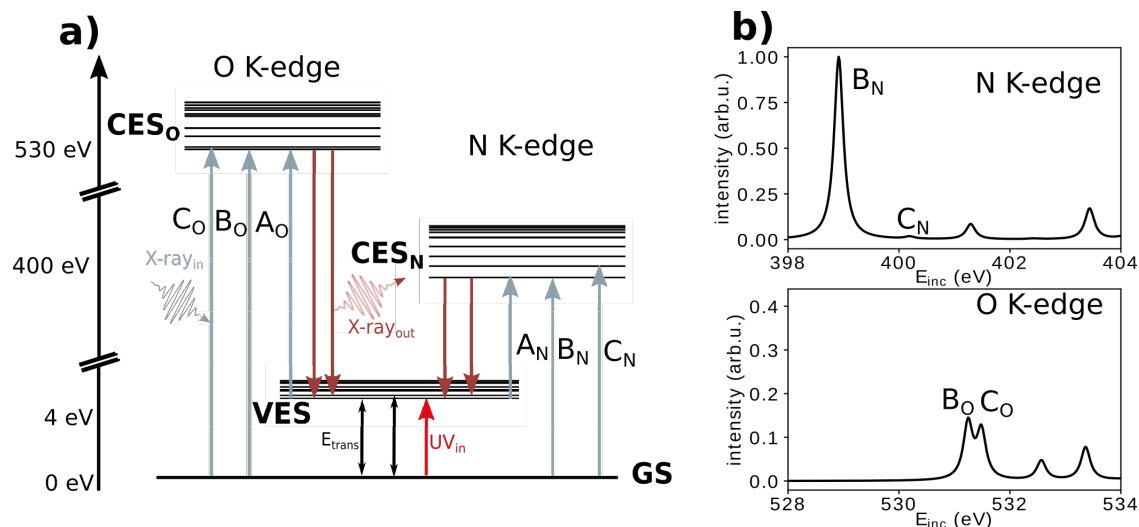
Figure 2. a) Schematic showing the transitions in transient RIXS. The GS describes the system in an unperturbed state and is used as common reference for all other transitions. X-ray excitation (X-ray$_{in}$) at the N or O K-edge leads to population of CES$_N$ or CES$_O$, respectively, (grey arrows). Relaxation from the CES to the VES causes emission of X-ray$_{out}$ (dark red). The energy transfer (energy difference between X-ray$_{in}$ and X-ray$_{out}$) describes the energy of the VES in comparison to the GS. b) Simulated XANES spectra of HBQ at the N and O K-edges. Spectra are normalized to the N K-edge spectrum.

105 often divided into two regions depending on the character of the CESs accessed in the

106 experiment.[32,47,59] The contributions of the four highest occupied, and lowest unoccupied

107 molecular orbitals to the different CESs and VESs are tabulated in Table S1 and Table S2

108 and the molecular orbitals are pictured in Fig. S4 of the SI. Based on the contributions from

109 the different molecular orbitals, the lowest CESs are of π character while the CESs involved

110 in transitions above $401\,\text{eV}$ at the N K-edge and above $534\,\text{eV}$ at the O K-edge are of σ

111 character. In the following discussion, we will focus on the π transitions which have been

112 resolved experimentally for organic molecules.[59]

113 The 2D GS RIXS maps of the enol form of HBQ at the N and O K-edge are presented

114 in Fig. 3c and d. The RIXS maps are plotted as energy transfer (E_{trans}) vs. incident energy

115 (E_{inc}) where the energy transfer is the difference between incoming and emitted X-ray photon

116 energy $E_{trans} = E_{inc} - E_{emi}$. Features at $E_{trans} = 0$ correspond to elastic scattering in the

117 system of interest. Additional features in the RIXS spectra arise from inelastic scattering

118 and can give insights into the coupling between the ith intermediate state or CES$_{N,i}$ and the

6

^{119} fth final states or VES$_f$ involved in the RIXS process. The major peaks along the incident

^{120} energy axis of the RIXS map result from excitation into the CESs and correspond to X-ray

^{121} absorption features. These peaks are labelled B and C following our previous study.[8]

^{122} At the N K-edge, the B (399 eV) and C (401.3 eV) peaks correspond to excitations from

^{123} the GS into CES$_{N,1}$ and CES$_{N,2}$ states, respectively, and are represented by the grey arrows

^{124} in Fig. 2a. The B peak is the strongest transition visible in the spectrum. The high oscillator

^{125} strength of excitation from the GS into CES$_{N,1}$ (B peak) can be explained by the strong

^{126} overlap between the N1s and $1\pi^*$ orbitals, which is greater than the overlap between the

^{127} N1s and the $2\pi^*$ orbital, which is the main contributor to CES$_{N,2}$ (see Table S1 in the SI),

^{128} resulting in the weaker oscillator strength of the C peak. The discussion of the cross peaks

^{129} in the GS RIXS map will focus on a few strong inelastic features labelled in Fig. 3c. The

^{130} different features will be labelled according to excitation into a CES and relaxation into a

^{131} VES f. For example, B$_I^f$ corresponds to excitation into CES$_1$ (B-peak) and relaxation into

^{132} VES f at the K-edge of atom I. For B$_N^1$ and for B$_N^3$ core excitation takes place into CES$_{N,1}$

^{133} and followed by relaxation into the VES$_1$ or VES$_3$ leading to emission. B$_N^3$ at $E_{inc} =$399 eV

^{134} and $E_{trans} =$4.7 eV is the strongest feature in the N K-edge RIXS map. Other contributions

^{135} to the RIXS spectrum at the N K-edge have significantly lower oscillator strengths and will

^{136} not be discussed further here. Oscillator strengths for all RIXS features are listed in Table S3

^{137} of the SI.

^{138} For a more quantitative analysis of the RIXS spectrum, we will next consider different

^{139} spectral cuts through the RIXS maps. These spectral cuts are indicated in Fig. 3c as lines

^{140} in the RIXS map and plotted in Fig. 3a and Fig. 3b for the N K-edge. In Fig. 3a, partial

^{141} fluorescence yield (PFY) XANES spectra, obtained by integrating along the emission axis,

^{142} are compared to high energy resolution fluorescence detected (HERFD) XANES spectra,

^{143} corresponding to cuts at constant emission energies (see diagonal dashed line in Fig. 3c). In

^{144} transition metal systems, HERFD-XANES cuts are often used to increase spectral resolution

^{145} which unlike the XANES spectral resolution is not limited by the core-hole lifetime but

7

146 rather by the final-state lifetime.[60,61] Due to the already small lifetime broadening in lighter

147 atoms like N and O, HERFD-XANES does not lead to an increased resolution in our study.

148 However, there are distinct differences between the HERFD- and PFY-XANES spectra due

149 to their different projections on the incident energy axis. At the N K-edge, the spectral

150 positions of the features along the E_{inc} axis do not change, however the intensity of the C

151 peak, decreases in the HERFD-XANES spectrum relative to the PFY-XANES spectrum.

152 Insights into the different VESs that are coupled to excitation to a specific CES, are

153 encoded in the energy transfer transfer axis and are analyzed using constant incident energy

154 (CIE) spectral cuts. Fig. 3b shows the CIE spectra at the N K-edge along the incident

155 energies for both the B (black, $E_{inc} = 399\,eV$) and C (grey, $E_{inc} = 401.3\,eV$) peaks. The CIE

156 spectra directly report on the transition energies and coupling amplitudes between occupied

157 and unoccupied VESs, similar to UV/vis spectra, but with different selection rules.[62] At

158 the N K-edge, the CIE spectra (see Fig. 3b) taken along the B_N and C_N peaks show a

159 signal at $4.6\,eV$ representing a transition to VES_3. For the CIE spectra along the C_N peak

160 we observe an additional feature from transition into VES_4 at $E_{trans} = 5.3\,eV$. From the

161 varying amplitudes of the spectral features in the CIE spectra we glean that there is strong

162 coupling of $CES_{N,1}$ to VES_3 and of $CES_{N,2}$ to VES_4. The couplings of the CESs to other

163 final states are very weak as evidenced by the absence of additional peaks in the CIE spectra

164 at the N K-edge.

165 The GS RIXS map for enolic HBQ at the O K-edge is presented in Fig. 3d. The B_O and

166 C_O peaks (arising from excitation into $CES_{O,1}$ and $CES_{O,2}$) around $531.5\,eV$ are of similar

167 intensity and are split by $0.2\,eV$. Fig. 3e shows the comparison of HERFD- and PFY-XANES

168 spectra at the O K-edge. The relative intensities between the B_O and C_O peaks drastically

169 change between the two spectra reflecting their different projections along the incident energy

170 axis emphasising coupling to different VESs. The CIE spectral cuts along $E_{inc} = 531.2\,eV$

171 and $E_{inc} = 531.5\,eV$ at the O K-edge are presented in Fig. 3f. These spectra display several

172 cross-peaks highlighting the coupling of several VESs with $CES_{O,1}$ and $CES_{O,2}$. The CIE

8

cuts taken at B_O and C_O show features at $3.8\,\text{eV}$ and at $4\,\text{eV}$, corresponding to a transition into VES_1 and VES_2, respectively. Two additional features at $4.8\,\text{eV}$ and $5.2\,\text{eV}$ are higher in intensity and correspond to transition into VES_3 and VES_4, respectively.
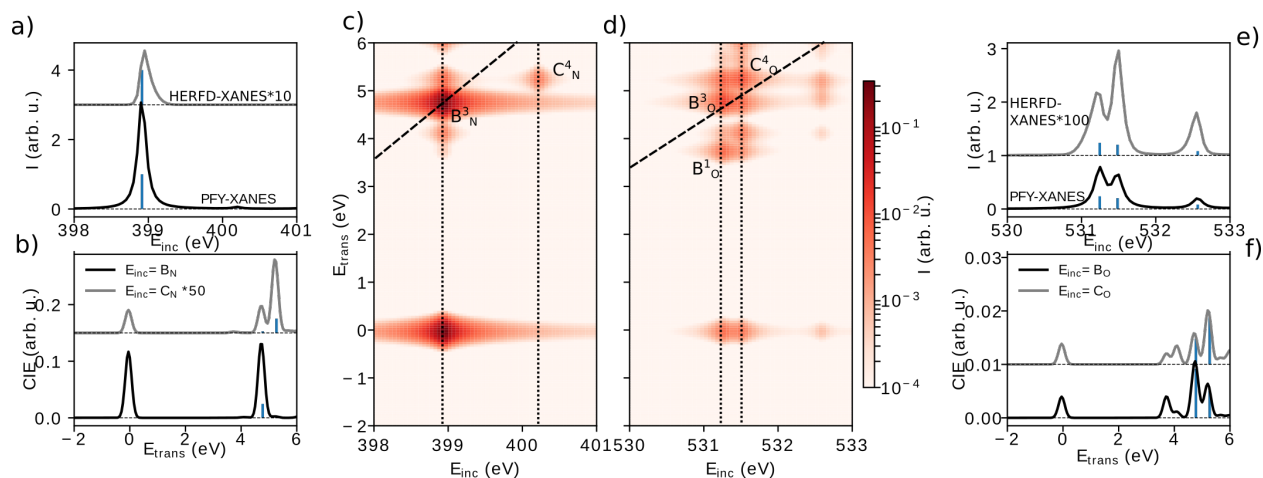
Figure 3. Ground state RIXS of HBQ in its enol form at the N (a-c) and O K-edge (d-f). c) RIXS map of HBQ at the N K-edge. d) RIXS map of HBQ at the O K-edge. a,e) PFY- and HERFD-XANES spectra. HERFD-XANES cuts are indicated by the diagonal dashed lines in the RIXS maps. b,f) Constant Incident Energy (CIE) cuts along the B peak (black) and C peak (grey). The cuts are marked by the vertical dotted lines in the 2D RIXS maps.

A comparison of the XANES spectra at the N and O K-edges (see Fig. 2) highlights the small relative energy difference between the B and C peaks at the O K-edge compared to the N K-edge. The difference between the two absorption edges can be explained by taking a close look at the contributing molecular orbitals to the two CESs presented in Table S1 in the SI. From the table, we see that the transitions to $CES_{N,1}$ and $CES_{N,2}$ have strong contributions by the $1\pi^*$ and $2\pi^*$ orbitals, respectively. This is in contrast to the transitions to $CES_{O,1}$ and $CES_{O,2}$ where the $1\pi^*$ and $2\pi^*$ orbitals contributing equally to both states. The mixed character of the CESs at the O K-edge causes the B_O and C_O peaks to be closer in energy. The smaller oscillator strengths of the XANES spectral features at the O K-edge compared to the N K-edge are caused by the small overlap between the O1s and $1\pi^*$ and $2\pi^*$ orbitals which mainly contribute to the $CES_{I,1}$, $CES_{I,2}$, in contrast the overlap of the π^* orbitals with the N1s. A comparison of the HERFD-XANES and the PFY-XANES spectra at the N (Fig. 3a,b) and O (Fig. 3e,f) K-edges, reveals changes in relative intensities

9

of the spectral features. These differences are strongly dependent on the chosen emission energy at which the cut is taken, as shown in the SI (Fig. S6) and a direct comparison between HERFD-XANES and XANES features should always be performed with caution. However, the changes in relative intensities in HERFD spectra compared to XANES can help in disentangling different contributions to the RIXS spectra.

We can compare the strongest transition in energy transfer axis for the O and N K-edges by looking at their CIE spectral cuts along the B and C peaks (Figs. 3b and c). Due to the mixed character of the CESs at the O K-edge, we observe strong coupling to several VESs , which gives rise to the B_O^{1-4} and C_O^{1-4} features with similar spectral intensities while at the N K-edge we predominantly observe features from only one transition, B_N^3. The different cross-peak intensities at the N and O K-edges show variation in couplings between different electronic states depending on which atom is being investigated.

The above analysis of the calculated GS RIXS maps of HBQ at the O and N K-edges highlights how we can disentangle the VESs coupled to CESs and thereby gain insights into the character of the contributing molecular orbitals and into the electronic charge distribution across the intramolecular H-bond. The relationship between X-ray spectral signatures and H-bonding strengths has been discussed for imidazole[28] and acetic acid.[59] In the SI (Fig. S3), we present calculated RIXS spectra of HBQ in its keto form as a limiting case for how the proton transfer impacts the local electronic structure at the H-donor and acceptor atoms. We also refer the reader to the discussion in the SI accompanying Fig. S3 and of the calculated XANES spectrum for the GS HBQ keto form published earlier.[8] In brief, we observe that increased NH-bond strength leads to a blue-shift at the N K-edge and an increased OH-bond strength leads to a blue-shift at the O K-edge. This can be attributed to a lowering in energy of the corresponding 1s orbital which has previously been employed to distinguish the two tautomers of 3-hydroxypyridine.[47] The cross-peaks in the RIXS maps show an overall red-shift of the spectral features in the energy transfer axis and larger energy differences between the different transitions (see Fig. S3). The red-shift of the features along the energy transfer

10

axis can be explained by the smaller gap between GS and first VES in the keto form as schematically presented in Fig. 1.

The position and amplitude of the peaks in the the RIXS spectra of HBQ highlight the detailed electronic state coupling information that can be gained from the RIXS experiment as compared to our previous XANES study. Due to the underlying processes, XANES is only sensitive to CESs. In the RIXS process, the energy transfer axis contains additional information on VESs and most importantly on the coupling between the CESs and VESs at different atomic sites. In other words, the RIXS maps provide a complete mapping of the electronic energy landscape revealing the occupied and unoccupied electronic states, which dictate the (photo)chemical properties of a system. Additionally, a comparison of the molecular orbitals involved in the different RIXS transitions give insights into how the local electron densities impact the intramolecular H-bond in HBQ. In the following, we will show how excited state RIXS can be used to directly follow the reorganization of the electronic states in HBQ during and following ESIPT.

For computing the evolution of RIXS spectra during and following the ESIPT process, we performed MD simulations on the first VES for 180 fs. Structures along the VES trajectory were sampled in 1.2 fs intervals. The structural dynamics show that ESIPT takes place after 12 fs which is in good agreement with experimental studies.[19,20] Transient RIXS maps were calculated in 6 fs intervals on the VES_1. We note that the analysis presented below is based on a single trajectory. To confirm that the interpretation of the VES RIXS maps is not biased by analysis of a single trajectory, we have compared the structural dynamics of 26 different trajectories, presented in the SI. The averaged results of atomic distances from the calculations of the multiple trajectories confirms that vibrational coherence on the first VES of HBQ following ESIPT survives averaging of 26 trajectories as presented in the SI Fig. S7.

Figures 4a-c show transient RIXS maps at the N K-edge calculated for structures sampled at 0 fs, 7 fs, and 165 fs, respectively. Since the proton transfer takes place within 12 fs, the RIXS map at 0 fs shows signals from molecules on the E* state. The RIXS map at 7 fs is
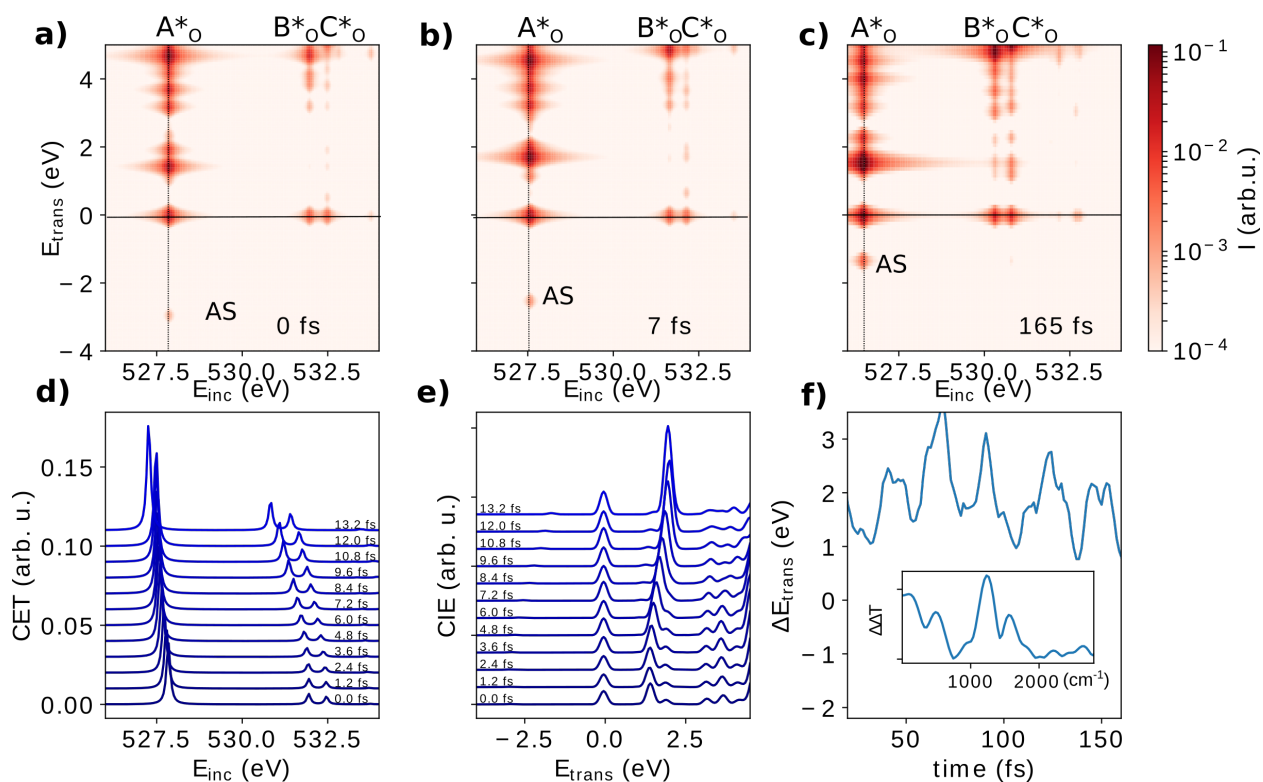
11
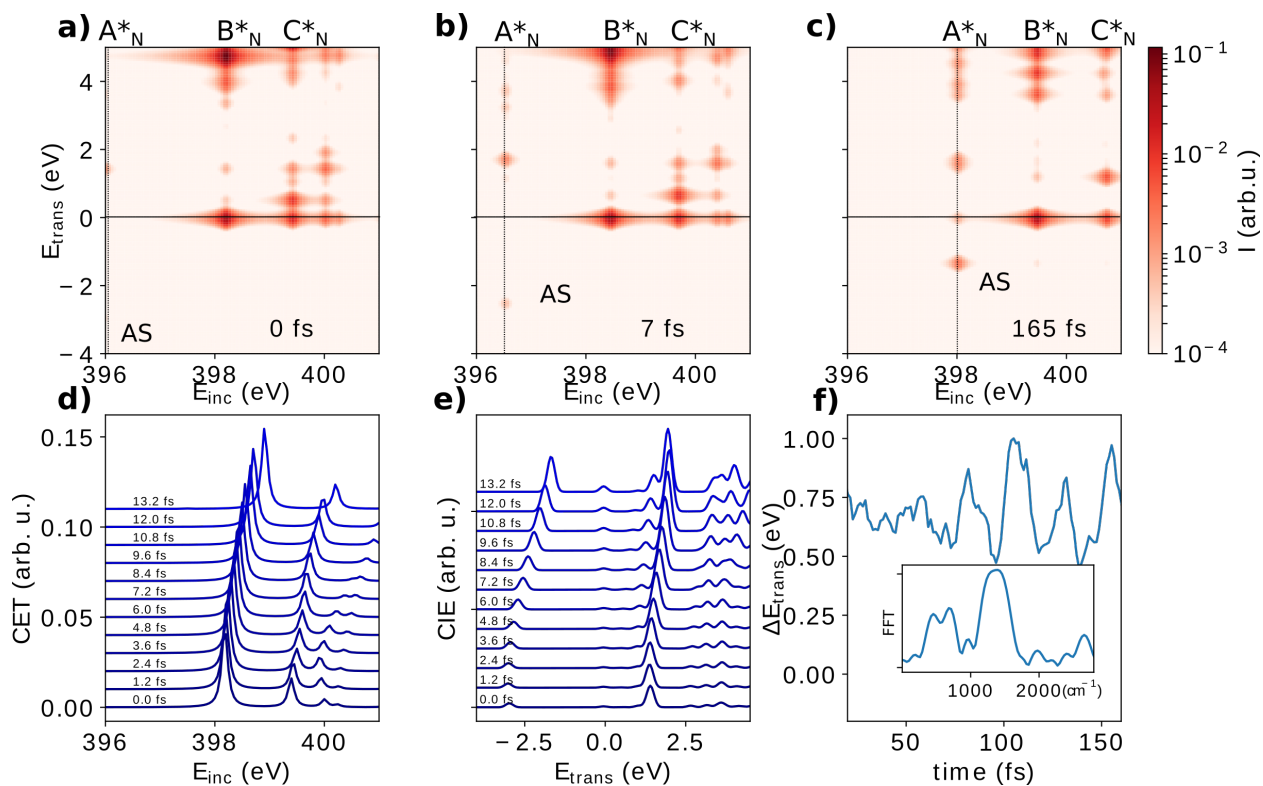
Figure 4. Transient RIXS features at the N K-edge: a-c) Transient RIXS maps calculated for structures on the first VES after 0 fs, 7 fs and 165 fs. d) Transient CET cuts along the elastic line (indicated by horizontal lines in the 2D maps) and e) Transient CIE cuts of the A peak (vertical lines in 2D maps) for selected timepoints during the proton transfer. f) Amplitude of the anti-Stokes feature (AS) as a function of time. The inset plots the FFT amplitude of the oscillatory features.

12

representative of a molecule undergoing ESIPT, and the RIXS map at 165 fs is representative of a molecule in the K* state following proton transfer. As previously observed in the calculated transient XANES spectra,[8] an additional A_N^* peak appears to the red of the B_N^* and C_N^* peaks along the incident energy. This feature corresponds to core excitation from VES_1 into $CES_{N,1}^*$, simulating RIXS spectra after laser excitation (UV_{in} in Fig. 1b) and is $1\,eV$ to the red of the B_N^* peak. We also observe the appearance of a weak feature at negative energy transfer energies ($-4\,eV$ to $-1.5\,eV$) which we will refer to as the anti-Stokes feature in the following. The anti-Stokes feature corresponds to excitation from the VES (VES_1) into the $CES_{I,1}^*$ state and subsequent relaxation into the GS. Such features at negative energy transfer have previously been experimentally observed in time-resolved RIXS studies at the N K- and Fe L-edges of metal complexes.[53,54]

In order to understand the time-dependence of the RIXS features during ESIPT, we look at spectral cuts during 0 fs to 13 fs. The constant energy transfer (CET) spectral cuts along the elastic line are presented in 4d and we see that the B_N and C_N move to higer incident energies reflecting the change in electron density across the intramolecular H bond, as the proton moves from the O to the N atom. Fig. 4e presents the CIE spectral cuts along the A_N^* peak during ESIPT. We observe a strong blue-shift of the CIE features during ESIPT. The strongest feature appears at $1.5\,eV$ and shifts towards $1.8\,eV$. This feature can be assigned to the energy transfer from VES_4 to VES_1, highlighting the time-evolving increase in energy difference between the different VESs during ESIPT. The intensity of the spectral feature at $1.5\,eV$ increases during ESIPT reflecting the changing overlap in electron density between GS and CES orbitals as the proton transfers to the nitrogen atom.

Fig. 5 displays the transient RIXS maps and spectral cuts for the O K-edge. Panels a-c present the 2D RIXS maps at 0 fs, 7 fs, and 165 fs. Similiar to the N K-edge, an additional peak, A_O^*, appears at $5.5\,eV$ to the red of the B_O peak. The B_O^* and C_O^* peaks are blue-shifted by about $1\,eV$ compared to their GS positions, emphasising the effect of valence excitation not only on the VESs but also the CESs. Fig. 5d shows the CET spectral cuts

13

Figure 5. Transient RIXS features at the O K-edge: a-c) Transient RIXS maps calculated for structures of the first VES after 0 fs, 7 fs and 165 fs. d) Transient CET cuts along the elastic line (indicated by horizontal lines in the 2D maps) and e) transient CIE cuts of the A peak (vertical lines in 2D maps) for selected timepoints during the proton transfer. f) Amplitude of the anti-Stokes feature (AS) as a function of time. The inset plots the FFT amplitude of the oscillatory features.

14

along the elastic line at the O K-edge, presenting a shift towards lower incident energies, corresponding to a decrease in energy of the CES*s during ESIPT. Fig. 5e shows the CIE spectral cuts along the A_O^* peak at the O K-edge, presenting the same trends as at the N K-edge with the strongest feature at $1.5\,\text{eV}$ corresponding to transition from VES_4 to VES_1. This peak shifting towards $1.8\,\text{eV}$ and increases in intensity during the first $13\,\text{fs}$ reflecting the reorganization of the VESs and the time evolving electron density overlap between the CES and the GS during ESIPT.

Comparing the transient RIXS spectra at the N and O K-edges, the A peak has a much stronger intensity at the O K-edge compared to the N K-edge. These differences in intensity can be explained by the stronger overlap between VES_1 (the initial state of the RIXS process after photoexcitation) and $CES_{O,1}^*$ than $CES_{N,1}^*$. The increase/decrease in energy of the intermediate states observed through the shifts of the peaks in the CET spectral cuts at the N and O K-edge, respectively, is linked to stabilisation of the atom-specific GS upon formation of a H-bond. At the N K-edge, we additionally observe an increase in A_N^*, B_N^* and C_N^* in the CET spectral cuts, while there is a slight decrease in these energy differences at the O K-edge. The CIE spectral cuts (Fig. 4e and Fig. 5e) describe the same states (VES) at both absorption edges, the peak positions and energy changes are the same at the N and O K-edge, however the amplitudes are different. Looking at the 2D RIXS maps at the N K-edge, we observe that the relative intensity of the cross peaks compared to the GS increases during ESIPT and decreases following ESIPT. The opposite trend is observed at the O K-edge. This highlights that the dynamic states are highly coupled at N K-edge but less so at the O K-edge.

The dynamics of the transient RIXS signals can be investigated in more detail by integrating the anti-Stokes feature and following its intensity and position as function of time. Since the anti-Stokes feature is spectrally isolated and contains information on both CES, and VES, it is ideally suited to monitor the dynamics during and following ESIPT. The oscillations in intensity following ESIPT at both the N and O absorption edges are presented

15

in Fig. 4f and Fig. 5f with the Fourier transform in the insets. Even though the anti-Stokes features at both absorption edges describe the coupling to the same VESs, the strength of this coupling depends on the absorption edge. The insets of Figs. 4 and 5 display the Fourier Transform amplitudes of the oscillations in the intensity of the anti-Stokes feature at the N and O K-edge respectively. To shed light on how the electronic structure at the N and O K-edges is modulated by the observed frequencies, a comparison with the excited-state normal modes of the K* state was made. See descriptions of the vibrations in Fig. S11 in the SI. The vibrations between $1000\,\mathrm{cm}^{-1}$ to $2000\,\mathrm{cm}^{-1}$ correspond to backbone vibrations including carbonyl stretching and N–H bending. We are limited to observing vibrations within the $450\,\mathrm{cm}^{-1}$ to $2800\,\mathrm{cm}^{-1}$ range given the sampling rate and length of the MD simulations. It is worth noting that vibrational coherences have been observed in time resolved optical experiments of HBQ, but those have focused on vibrations below $1000\,\mathrm{cm}^{-1}$.[11,63,64] Recently we have observed high frequency vibrational coherences in HBQ during and following proton transfer.[65]

We explore the time-dependent changes in the position of the anti-Stokes feature along the E_{inc} and E_{trans} axes at the N and O K-edges in Fig. S11 in the SI. We see an increase in the energy transfer energy of the anti-Stokes feature within $12\,\mathrm{fs}$ followed by oscillations of the spectral position at the N and O K-edges. The identical spectral changes at the O and N K-edges are due to the fact that the spectral shifts in the energy transfer axis are given by the energy differences between the VESs. We note that these oscillations will be different from those observed in an UV transient absorption due to different selection rules of the RIXS process.

Figure 6 further explores the correlation between the movement of the proton during ESIPT and the spectral position of the anti-Stokes feature along the E_{trans} axis. The proton movement is defined as $\Delta R = R(\mathrm{N-H}) - R(\mathrm{O-H})$. We observe a strong correlation between ΔR and the spectral position of the anti-Stokes feature within the first $12\,\mathrm{fs}$, i.e. during ESIPT where the structural changes are dominated by the proton transfer. During

16

the early time points the shift in E_{trans} of the anti-Stokes feature as a function of ΔR corresponds to the mapping of dynamic change in energy difference between GS and first VES moving from enol to keto HBQ as presented in Fig. 1 where the difference between GS and first VES decreases along the ESIPT reaction coordinate with a slope of $1.6\,\mathrm{eV\,\mathring{A}^{-1}}$. The "spectral ruler" in Fig. 6 demonstrates that the spectral changes linked to the structural changes are large enough to be detected with currently available experimental resolutions at XFEL endstations. From Fig. 6 we see that the correlation between E_{trans} of the anti-Stokes feature and ΔR is not valid following ESIPT because several vibrational modes in the molecule influence both structure and spectral signatures causing a break-down of the linear relationship. In the SI (Fig. S11) we present the correlation between structure and spectral shifts in incident energy and energy transfer for several features in the N and O K-edge RIXS maps, showing that a similar trend can be observed for all of them. However, the magnitude of the spectral changes depends on the investigated feature, highlighting that different states have varying sensitivity to the enol-keto transition. The comparison shows that the strongest spectral change is observed when looking at the changes in energy transfer of the anti-Stokes feature. This work highlights the potential of using transient RIXS spectroscopy to gain direct structural insight into structural dynamics on a molecular level.
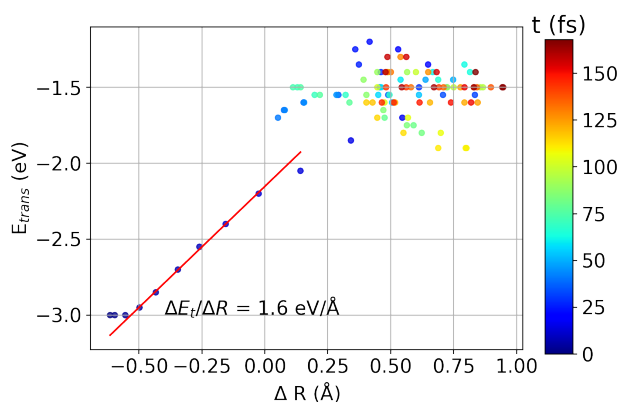
Figure 6. E_{trans} of the AS feature as function of $\Delta R = R(N-H) - R(O-H)$ from early time-points (blue) to late time-points (red). The red line shows a linear fit of the changes in E_{trans} within the $12\,\mathrm{fs}$, giving a slope of $1.6\,\mathrm{eV\,\mathring{A}^{-1}}$.

In this work, we have presented a study of GS and transient RIXS signals of an H-bonded

17

model complex, HBQ. Investigation of the GS spectra shows the potential of RIXS to fully map the electronic structure of a given system, including both core and valence excited states. Additionally, analysis of the cross peaks in the 2D RIXS maps gives important insights into the coupling between different electronic states which contains information on the contributing molecular orbitals. By considering RIXS maps from the perspective of the proton-donor (O) and -acceptor (N) atoms, the intricate coupling between electronic and atomic structure is revealed.

The time-resolved RIXS spectra show how structural changes affect the coupling between different states. The spectral changes in the RIXS maps can directly be correlated to structural changes during the proton transfer, giving a spectral 'ruler' to measure structural changes. By using and comparing different spectral features for this ruler, we gain insights into what affects the amplitude of spectral changes in X-ray spectroscopy and the sensitivity of different states to structural changes. The dynamic changes additionally reveal the vibrations underlying the ESIPT process.

With the new capabilities of soft X-ray endstations at high repetition rate XFELs, time-resolved RIXS studies, like presented here, will soon be possible experimentally and allow for direct observation of the intricate changes in electronic structure during ESIPT.

Computational Methods

All calculations were performed with the open-source NWChem computational chemistry program.[66–68] The ground-state (GS) HBQ geometry was optimized at the DFT level of theory using the PBE0 functional[69] and def2-TZVP basis set.[70] The solvent-environment of toluene was modelled using the COnductor-like Screening MOdel (COSMO)[71,72] with a dielectric constant of $\epsilon = 2.38$. UV/Vis spectra were computed at the TDDFT level of theory,[73] while the XANES spectra at the O and N K-edges were computed with the restricted energy window extension of TDDFT.[74] XANES spectra were shifted relative to

18

experimental data. Since no experimental spectra on HBQ were available, the shift was determined by performing calculations for 3-hydroxypyridine at the same level of theory and compare the results to experimental data from literature,[47] resulting in a shift of 11 eV (see SI). For this reason the spectra presented here are shifted compared to our previous work where spectra were not shifted to match experimental data.

RIXS calculations were performed using the Kramers–Heisenberg equation,[36]

$$\sigma(\omega', \omega) = \frac{\omega'}{\omega} \sum_{fi} |F_{fi}(\theta)| \left[\frac{(\omega_i \omega_f \alpha)^2}{(\omega - \omega_i)^2 + \Gamma_i^2/4} \right] \tag{1}$$

where the amplitude σ is a function of the incoming ω' and emitted photons ω with intermediate state i and final state f where ω_j and the lifetime Γ_j of state. RIXS spectra were simulated by coupling XANES and UV/Vis transitions following the protocol published earlier.[40,75] A lifetime broadening of 0.13 eV and 0.27 fs were applied for the core-excited state at the N and O K-edge, respectively, and of 0.13 eV for the valence-excited state at both absorption edges. In order to minimize the effects of elastic scattering, the angle between the polarization of the incoming photon and the propagation direction of the outgoing photon, θ, was set to zero.

For RIXS maps on the first VES, excited-state molecular dynamics simulations at the TDDFT level werw performed on VES$_1$ using analytical gradients.[76] Excited state simulations were run using the Gaussian basis set quantum molecular dynamics (QMD) module in NWChem[77] and 10 au (0.24 fs) timesteps. No thermostat was used. We ran 26 excited state trajectories starting from the optimised GS structure, simulating vertical excitation. For each trajectory different initial velocities were randomly selected from the Maxwell–Boltzmann distribution at room temperature (298.15 K). We did not employ surface hopping methods since the first and second VES are energetically well separated (by ≥ 0.5 eV) and the proton-transfer occurs on VES$_1$. Neither nuclear quantum effects[78] nor explicit dephasing effects[79] were included in our dynamics simulations.

19

We computed transient UV/vis, XANES, and RIXS spectra for geometries extracted every 2.4 fs from a single excited-state trajectory. As detailed in our previous publication, these computations on the first VES required three steps for each of the selected time points.[8] First, the ground-state molecular orbitals were obtained by converging the self-consistent field (SCF). Second, to simulate the HOMO-LUMO excitation of an electron, occupancy of the alpha HOMO and LUMO orbitals were swapped and the SCF reconverged. Third, spectra were computed based on the molecular orbitals for VES_1. The resulting broadened spectra are shown in Figs. 4 and 5.

Acknowledgement

References

(1) Weller, A. Innermolekularer Protonenübergang im angeregten Zustand. *Berichte der Bunsengesellschaft für physikalische Chemie* **1956**, *60*, 1144–1147.

(2) Zhao, J.; Ji, S.; Chen, Y.; Guo, H.; Yang, P. Excited state intramolecular proton transfer (ESIPT): From principal photophysics to the development of new chromophores and applications in fluorescent molecular probes and luminescent materials. *Physical Chemistry Chemical Physics* **2012**, *14*, 8803–8817.

(3) Kwon, J. E.; Park, S. Y. Advanced organic optoelectronic materials: Harnessing excited-state intramolecular proton transfer (ESIPT) process. *Advanced Materials* **2011**, *23*, 3615–3642.

(4) Jodra, A.; Marazzi, M.; Frutos, L. M.; García-Iriepa, C. Modulating Efficiency and Color of Thermally Activated Delayed Fluorescence by Rationalizing the Substitution Effect. *Journal of Chemical Theory and Computation* **2024**, acs.jctc.4c00009.

(5) Balasubramanian, M.; Reynolds, A.; Blair, T. J.; Khalil, M. Probing ultrafast vibrational dynamics of intramolecular hydrogen bonds with broadband infrared pump-probe spectroscopy. *Chemical Physics* **2019**, *519*, 38–44, Publisher: Elsevier.

(6) Chou, P. T.; Wei, C. Y. Photophysics of 10-hydroxybenzo[h]quinoline in aqueous solution. *Journal of Physical Chemistry* **1996**, *100*, 17059–17066.

(7) Lee, J.; Kim, C. H.; Joo, T. Active role of proton in excited state intramolecular proton transfer reaction. *Journal of Physical Chemistry A* **2013**, *117*, 1400–1405.

(8) Loe, C. M.; Liekhus-Schmaltz, C.; Govind, N.; Khalil, M. Spectral Signatures of Ultrafast Excited-State Intramolecular Proton Transfer from Computational Multi-edge Transient X-ray Absorption Spectroscopy. *The Journal of Physical Chemistry Letters* **2021**, *12*, 9840–9847.

21

(9) Chen, K. Y.; Hsieh, C. C.; Cheng, Y. M.; Lai, C. H.; Chou, P. T. Extensive spectral tuning of the proton transfer emission from 550 to 675 nm via a rational derivatization of 10-hydroxybenzo[h]quinoline. *Chemical Communications* **2006**, *1*, 4395–4397.

(10) Picconi, D. Nonadiabatic quantum dynamics of the coherent excited state intramolecular proton transfer of 10-hydroxybenzo[h]quinoline. *Photochemical and Photobiological Sciences* **2021**, *20*, 1455–1473, Publisher: Springer International Publishing ISBN: 0123456789.

(11) Takeuchi, S.; Tahara, T. Coherent nuclear wavepacket motions in ultrafast excited-state intramolecular proton transfer: Sub-30-fs resolved pump-probe absorption spectroscopy of 10-hydroxybenzo[h]quinoline in solution. *Journal of Physical Chemistry A* **2005**, *109*, 10199–10207.

(12) Zhou, M.; Zhao, J.; Cui, Y.; Wang, Q.; Dai, Y.; Song, P.; Xia, L. Theoretical study on the excited-state intramolecular proton-transfer reaction of 10-hydroxybenzo[h]quinoline in methanol and cyclohexane. *Journal of Luminescence* **2015**, *161*, 1–6.

(13) Chansen, W.; Salaeh, R.; Prommin, C.; Kerdpol, K.; Daengngern, R.; Kungwan, N. Theoretical study on influence of geometry controlling over the excited-state intramolecular proton transfer of 10-hydroxybenzo[h]quinoline and its derivatives. *Computational and Theoretical Chemistry* **2017**, *1113*, 42–51.

(14) Higashi, M.; Saito, S. Direct Simulation of Excited-State Intramolecular Proton Transfer and Vibrational Coherence of 10-Hydroxybenzo[h]quinoline in Solution. *The Journal of Physical Chemistry Letters* **2011**, *2*, 2366–2371.

(15) Kim, C. H.; Joo, T. Coherent excited state intramolecular proton transfer probed by time-resolved fluorescence. *Physical Chemistry Chemical Physics* **2009**, *11*, 10266–10269.

22

(16) Zhang, L.; Fassioli, F.; Fu, B.; She, Z. S.; Scholes, G. D. Modeling Excited-State Proton Transfer Using the Lindblad Equation: Quantification of Time-Resolved Spectroscopy with Mechanistic Insights. *ACS Physical Chemistry Au* **2023**, *3*, 107–118.

(17) Ilia Sokolovskii; Gerrit Groenhof Photochemical initiation of polariton-mediated exciton propagation. *Nanophotonics* **2024**, 1–8.

(18) Hristova, S.; Dobrikov, G.; Kamounah, F. S.; Kawauchi, S.; Hansen, P. E.; Deneva, V.; Nedeltcheva, D.; Antonov, L. 10-Hydroxybenzo[h]quinoline: switching between single- and double-well proton transfer through structural modifications. *RSC Advances* **2015**, *5*, 102495–102507.

(19) Lee, J.; Kim, C. H.; Joo, T. Active role of proton in excited state intramolecular proton transfer reaction. *Journal of Physical Chemistry A* **2013**, *117*, 1400–1405.

(20) Kim, C. H.; Joo, T. Coherent excited state intramolecular proton transfer probed by time-resolved fluorescence. *Physical Chemistry Chemical Physics* **2009**, *11*, 10266–10269.

(21) Piechowska, J.; Gryko, D. T. Preparation of a Family of 10-Hydroxybenzo[h]quinoline Analogues via a Modified Sanford Reaction and Their Excited State Intramolecular Proton Transfer Properties. *The Journal of Organic Chemistry* **2011**, *76*, 10220–10228.

(22) Lange, K. M.; Aziz, E. F. Electronic structure of ions and molecules in solution: a view from modern soft X-ray spectroscopies. *Chemical Society Reviews* **2013**, *42*, 6840.

(23) Smith, J. W.; Saykally, R. J. Soft X-ray Absorption Spectroscopy of Liquids and Solutions. *Chemical Reviews* **2017**, *117*, 13909–13934.

(24) Frati, F.; Hunault, M. O.; De Groot, F. M. Oxygen K-edge X-ray Absorption Spectra. *Chemical Reviews* **2020**, *120*, 4056–4110.

(25) Fujii, K.; Akamatsu, K.; Muramatsu, Y.; Yokoya, A. X-ray absorption near edge structure of DNA bases around oxygen and nitrogen K-edge. *Nuclear Instruments and Methods in Physics Research, Section B: Beam Interactions with Materials and Atoms* **2003**, *199*, 249–254.

(26) Wernet, P.; Nordlund, D.; Bergmann, U.; Cavalleri, M.; Odelius, M.; Ogasawara, H.; Naslund, L. A.; Hirsch, T. K.; Ojamae, L.; Glatzel, P.; Pettersson, L. G. M.; Nilsson, A. The Structure of the First Coordination Shell in Liquid Water. *Science* **2004**, *304*.

(27) Wilson, K. R.; Cavalleri, M.; Rude, B. S.; Schaller, R. D.; Catalano, T.; Nilsson, A.; Saykally, R. J.; Pettersson, L. G. X-ray absorption spectroscopy of liquid methanol microjets: Bulk electronic structure and hydrogen bonding network. *Journal of Physical Chemistry B* **2005**, *109*, 10194–10203.

(28) Das, S. K.; Winghart, M.-o.; Han, P.; Rana, D.; Zhang, Z.-y.; Eckert, S.; Fondell, M.; Schnappinger, T.; Nibbering, E. T. J.; Odelius, M. Electronic Fingerprint of the Protonated Imidazole Dimer Probed by X-ray Absorption Spectroscopy. *The Journal of Physical Chemistry Letters* **2024**, 1264–1272.

(29) Stetina, T. F.; Clark, A. E.; Li, X. X-ray absorption signatures of hydrogen-bond structure in water–alcohol solutions. *International Journal of Quantum Chemistry* **2019**, *119*, 1–6.

(30) Al, M. Solvent effects and pH dependence of the X-ray absorption spectra of proline from electrostatic embedding quantum mechanics / molecular mechanics and mixed-reference spin-flip time-dependent density-functional theory. *Journal of Physical Chemistry A* **2023**, ISBN: 0000000221.

(31) Eckert, S.; Vaz Da Cruz, V.; Ochmann, M.; Von Ahnen, I.; Föhlisch, A.; Huse, N. Breaking the Symmetry of Pyrimidine: Solvent Effects and Core-Excited State Dynamics. *Journal of Physical Chemistry Letters* **2021**, 8637–8643.

24

(32) Savchenko, V.; Eckert, S.; Fondell, M.; Mitzner, R.; Vaz da Cruz, V.; Föhlisch, A. Electronic structure, bonding and stability of fumarate, maleate, and succinate dianions from X-ray spectroscopy. *Physical Chemistry Chemical Physics* **2024**, *26*, 2304–2311.

(33) Wernet, P. et al. Orbital-specific mapping of the ligand exchange dynamics of Fe(CO)5 in solution. *Nature* **2015**, *520*, 78–81.

(34) Fransson, T.; Harada, Y.; Kosugi, N.; Besley, N. A.; Winter, B.; Rehr, J. J.; Pettersson, L. G. M.; Nilsson, A. X-ray and Electron Spectroscopy of Water. *Chemical Reviews* **2016**, *116*, 7551–7569.

(35) De Groot, F. M. F.; Haverkort, M. W.; Elnaggar, H.; Juhin, A.; Zhou, K.-J.; Glatzel, P. Resonant inelastic X-ray scattering. *Nature Reviews Methods Primers* **2024**, *4*, 45.

(36) Kramers, H. A.; Heisenberg, W. Über die Streuung von Strahlung durch Atome. *Zeitschrift für Physik* **1924**, 681–708.

(37) Gel'mukhanov, F.; Ågren, H. Resonant inelastic x-ray scattering with symmetry-selective excitation. *Physical Review A* **1994**, *49*, 4378.

(38) Gel'mukhanov, F.; Ågren, H. Resonant X-ray Raman scattering. *Physics Reports* **1999**, *312*, 87–330.

(39) Rehn, D. R.; Dreuw, A.; Norman, P. Resonant Inelastic X-ray Scattering Amplitudes and Cross Sections in the Algebraic Diagrammatic Construction/Intermediate State Representation (ADC/ISR) Approach. *Journal of Chemical Theory and Computation* **2017**, *13*, 5552–5559.

(40) Nascimento, D. R.; Biasin, E.; Poulter, B. I.; Khalil, M.; Sokaras, D.; Govind, N. Resonant Inelastic X-ray Scattering Calculations of Transition Metal Complexes within a Simplified Time-Dependent Density Functional Theory Framework. *Journal of Chemical Theory and Computation* **2021**, *17*, 3031–3038.

(41) Bergmann, U.; Wernet, P.; Glatzel, P.; Cavalleri, M.; Pettersson, L. G.; Nilsson, A.; Cramer, S. P. X-ray Raman spectroscopy at the oxygen K edge of water and ice: Implications on local structure models. *Physical Review B - Condensed Matter and Materials Physics* **2002**, *66*, 1–4.

(42) Vaz da Cruz, V. et al. Probing hydrogen bond strength in liquid water by resonant inelastic X-ray scattering. *Nature Communications* **2019**, *10*, 1–9.

(43) Weinhardt, L.; Benkert, A.; Meyer, F.; Blum, M.; Wilks, R. G.; Yang, W.; Bär, M.; Reinert, F.; Heske, C. Nuclear dynamics and spectator effects in resonant inelastic soft x-ray scattering of gas-phase water molecules. *The Journal of Chemical Physics* **2012**, *136*.

(44) Fouda, A. E.; Purnell, G. I.; Besley, N. A. Simulation of Ultra-Fast Dynamics Effects in Resonant Inelastic X-ray Scattering of Gas-Phase Water. *Journal of Chemical Theory and Computation* **2018**, *14*, 2586–2595.

(45) Wernet, P.; Testemale, D.; Hazemann, J. L.; Argoud, R.; Glatzel, P.; Pettersson, L. G.; Nilsson, A.; Bergmann, U. Spectroscopic characterization of microscopic hydrogen-bonding disparities in supercritical water. *Journal of Chemical Physics* **2005**, *123*.

(46) Guo, J.; Luo, Y. Molecular structure in water and solutions studied by photon-in/photon-out soft X-ray spectroscopy. *Journal of Electron Spectroscopy and Related Phenomena* **2010**, *177*, 181–191.

(47) Vaz da Cruz, V.; Büchner, R.; Fondell, M.; Pietzsch, A.; Eckert, S.; Föhlisch, A. Targeting Individual Tautomers in Equilibrium by Resonant Inelastic X-ray Scattering. *The Journal of Physical Chemistry Letters* **2022**, *13*, 2459–2466.

(48) Kunnus, K.; Josefsson, I.; Schreck, S.; Quevedo, W.; Miedema, P.; Techert, S.; De Groot, F.; Föhlisch, A.; Odelius, M.; Wernet, P. Quantifying covalent interactions

26

with resonant inelastic soft X-ray scattering: Case study of Ni2+ aqua complex. *Chemical Physics Letters* **2017**, *669*, 196–201.

(49) Eckert, S. et al. Ultrafast Independent N-H and N-C Bond Deformation Investigated with Resonant Inelastic X-Ray Scattering. *Angewandte Chemie - International Edition* **2017**, *56*, 6088–6092.

(50) Ge, G.; Zhang, J.-R.; Wang, S.-Y.; Wei, M.; Ji, Y.; Duan, S.; Ueda, K.; Hua, W. Mapping Hydrogen Positions along the Proton Transfer Pathway in an Organic Crystal by Computational X-ray Spectra. *The Journal of Physical Chemistry Letters* **2024**, 6051–6061.

(51) Barlow, K.; Phelps, R.; Eng, J.; Katayama, T.; Sutcliffe, E.; Coletta, M.; Brechin, E. K.; Penfold, T. J.; Johansson, J. O. Tracking nuclear motion in single-molecule magnets using femtosecond X-ray absorption spectroscopy. *Nature Communications* **2024**, *15*, 4043.

(52) Jay, R. M. et al. Disentangling Transient Charge Density and Metal-Ligand Covalency in Photoexcited Ferricyanide with Femtosecond Resonant Inelastic Soft X-ray Scattering. *Journal of Physical Chemistry Letters* **2018**, *9*, 3538–3543.

(53) Kunnus, K. et al. Anti-Stokes resonant x-ray Raman scattering for atom specific and excited state selective dynamics. *New Journal of Physics* **2016**, *18*, 103011.

(54) Jay, R. M. et al. Following Metal-to-Ligand Charge-Transfer Dynamics with Ligand and Spin Specificity Using Femtosecond Resonant Inelastic X-ray Scattering at the Nitrogen K-Edge. *The Journal of Physical Chemistry Letters* **2021**, *12*, 6676–6683.

(55) Freibert, A.; Mendive-Tapia, D.; Huse, N.; Vendrell, O. Time-Dependent Resonant Inelastic X-ray Scattering of Pyrazine at the Nitrogen K-Edge: A Quantum Dynamics Approach. *Journal of Chemical Theory and Computation* **2023**,

27

(56) Tanaka, S.; Volkov, S.; Mukamel, S. Time-resolved x-ray Raman spectroscopy of photoexcited polydiacetylene oligomer: A simulation study. *Journal of Chemical Physics* **2003**, *118*, 3065–3078.

(57) Schnack-Petersen, A. K.; Moitra, T.; Folkestad, S. D.; Coriani, S. New Implementation of an Equation-of-Motion Coupled-Cluster Damped-Response Framework with Illustrative Applications to Resonant Inelastic X-ray Scattering. *Journal of Physical Chemistry A* **2023**, *127*, 1775–1793.

(58) Soley, M. B.; Videla, P. E.; Nibbering, E. T.; Batista, V. S. Ultrafast Charge Relocation Dynamics in Enol-Keto Tautomerization Monitored with a Local Soft-X-ray Probe. *Journal of Physical Chemistry Letters* **2022**, *13*, 8254–8263.

(59) Savchenko, V. et al. Vibrational resonant inelastic X-ray scattering in liquid acetic acid: a ruler for molecular chain lengths. *Scientific Reports* **2021**, *11*, 1–8.

(60) Bauer, M. HERFD-XAS and valence-to-core-XES: new tools to push the limits in research with hard X-rays? *Phys. Chem. Chem. Phys.* **2014**, *16*, 13827–13837.

(61) Liekhus-Schmaltz, C. et al. Femtosecond X-ray Spectroscopy Directly Quantifies Transient Excited-State Mixed Valency. *The Journal of Physical Chemistry Letters* **2022**, 378–386.

(62) Stephen P. Cramer *X-Ray Spectroscopy with Synchrotron Radiation : Fundamentals and Applications*, 1st ed.; Biological and Medical Physics, Biomedical Engineering Series; Springer, 2020; pp 191–226.

(63) Kim, J. W.; Kim, C. H.; Burger, C.; Park, M.; Kling, M. F.; Kim, D. E.; Joo, T. Non-Born-Oppenheimer Molecular Dynamics Observed by Coherent Nuclear Wave Packets. *Journal of Physical Chemistry Letters* **2020**, *11*, 755–761.

(64) Schriever, C.; Barbatti, M.; Stock, K.; Aquino, A. J.; Tunega, D.; Lochbrunner, S.; Riedle, E.; de Vivie-Riedle, R.; Lischka, H. The interplay of skeletal deformations and ultrafast excited-state intramolecular proton transfer: Experimental and theoretical investigation of 10-hydroxybenzo[h]quinoline. *Chemical Physics* **2008**, *347*, 446–461.

(65) Sandwisch, J. PhD thesis, University of Washington, Seattle, WA, USA, 2023.

(66) Aprà, E. et al. NWChem: Past, present, and future. *J. Chem. Phys.* **2020**, *152*.

(67) Valiev, M.; Bylaska, E. J.; Govind, N.; Kowalski, K.; Straatsma, T. P.; Van Dam, H. J.; Wang, D.; Nieplocha, J.; Apra, E.; Windus, T. L.; De Jong, W. A. NWChem: A comprehensive and scalable open-source solution for large scale molecular simulations. *Computer Physics Communications* **2010**, *181*, 1477–1489, Publisher: Elsevier B.V.

(68) Nascimento, D. R.; Govind, N. Computational approaches for XANES, VtC-XES, and RIXS using linear-response time-dependent density functional theory based methods. *Physical Chemistry Chemical Physics* **2022**, *24*, 14680–14691, Publisher: Royal Society of Chemistry.

(69) Adamo, C.; Barone, V. Toward reliable density functional methods without adjustable parameters: The PBE0 model. *The Journal of chemical physics* **1999**, *110*, 6158–6170.

(70) Weigend, F.; Ahlrichs, R. Balanced basis sets of split valence, triple zeta valence and quadruple zeta valence quality for H to Rn: Design and assessment of accuracy. *Physical Chemistry Chemical Physics* **2005**, *7*, 3297–3305.

(71) Klamt, A.; Schüürmann, G. COSMO: a new approach to dielectric screening in solvents with explicit expressions for the screening energy and its gradient. *Journal of the Chemical Society, Perkin Transactions 2* **1993**, *0*, 799–805, Publisher: Royal Society of Chemistry.

29

(72) York, D. M.; Karplus, M. A Smooth Solvation Potential Based on the Conductor-Like Screening Model. *The Journal of Physical Chemistry A* **1999**, *103*, 11060–11079, Publisher: American Chemical Society.

(73) Hirata, S.; Head-Gordon, M. Time-dependent density functional theory within the Tamm–Dancoff approximation. *Chemical Physics Letters* **1999**, *314*, 291–299.

(74) Lopata, K.; Van Kuiken, B. E.; Khalil, M.; Govind, N. Linear-Response and Real-Time Time-Dependent Density Functional Theory Studies of Core-Level Near-Edge X-Ray Absorption. *Journal of Chemical Theory and Computation* **2012**, *8*, 3284–3292.

(75) Biasin, E.; Nascimento, D. R.; Poulter, B. I.; Abraham, B.; Kunnus, K.; Garcia-Esparza, A. T.; Nowak, S. H.; Kroll, T.; Schoenlein, R. W.; Alonso-Mori, R.; Khalil, M.; Govind, N.; Sokaras, D. Revealing the bonding of solvated Ru complexes with valence-to-core resonant inelastic X-ray scattering. *Chemical Science* **2021**, *12*, 3713–3725, Publisher: Royal Society of Chemistry.

(76) Silverstein, D. W.; Govind, N.; Van Dam, H. J.; Jensen, L. Simulating one-photon absorption and resonance Raman scattering spectra using analytical excited state energy gradients within time-dependent density functional theory. *Journal of chemical theory and computation* **2013**, *9*, 5490–5503.

(77) Fischer, S. A.; Ueltschi, T. W.; El-Khoury, P. Z.; Mifflin, A. L.; Hess, W. P.; Wang, H.-f.; Cramer, C. J.; Govind, N. Infrared and Raman Spectroscopy from *Ab Initio* Molecular Dynamics and Static Normal Mode Analysis: The CH Region of DMSO as a Case Study. *J. Phys. Chem. B* **2016**, *120*, 1429.

(78) Markland, T. E.; Ceriotti, M. Nuclear quantum effects enter the mainstream. *Nature Reviews Chemistry* **2018**, *2*, 0109.

(79) Mukamel, S. *Principles of nonlinear optical spectroscopy*; Oxford University Press on Demand, 1999.

Supporting Information Available

Supporting information is available.

31

TOC Graphic